PROCEEDINGS A

royalsocietypublishing.org/journal/rspa

Research



Cite this article: Jin H, Landauer AK, Kim K-S. 2021 Ruga mechanics of soft-orifice closure under external pressure. *Proc. R. Soc. A* **477**: 20210238.

https://doi.org/10.1098/rspa.2021.0238

Received: 14 March 2021 Accepted: 13 April 2021

Subject Areas:

mechanics, mechanical engineering

Keywords:

soft-material, ruga mechanics, bilayer-orifice buckling, symmetry breaking, closure resistance

Author for correspondence:

Kyung-Suk Kim

e-mail: kyung-suk_kim@brown.edu

Ruga mechanics of soft-orifice closure under external pressure

Hanxun Jin, Alexander K. Landauer and Kyung-Suk Kim

School of Engineering, Brown University, Providence, RI 02912, USA

(i) HJ, 0000-0001-7226-533X; AKL, 0000-0003-2863-039X; K-SK, 0000-0003-0681-346X

Here, we report the closure resistance of a softmaterial bilayer orifice increases against external pressure, along with ruga-phase evolution, in contrast to the conventional predictions of the matrixfree cylindrical-shell buckling pressure. Experiments demonstrate that the generic soft-material orifice creases in a threefold symmetry at a limit-load pressure of $p/\mu \approx 1.20$, where μ is the shear modulus. Once the creasing initiates, the triple crease wings gradually grow as the pressure increases until the orifice completely closes at $p/\mu \approx 3.0$. By contrast, a stiff-surface bilayer orifice initially wrinkles with multifold symmetry mode and subsequently develops ruga-phase evolution, progressively reducing the orifice cross-sectional area as pressure increases. The buckling-initiation mode is determined by the layer's thickness and stiffness, and the pressure by two types of the layer's instability modes—the surface-layer-wrinkling mode for a compliant and the ring-buckling mode for a stiff layer. The ringbuckling mode tends to set the twofold symmetry for the entire post-buckling closure process, while the high-frequency surface-layer-wrinkling mode evolves with successive symmetry breaking to a final closure configuration of two- or threefold symmetry. Finally, we found that the threefold symmetry mode for the entire closure process provides the orifice's strongest closure resistance, and human saphenous veins remarkably follow this threefold symmetry ruga evolution pathway.

1. Introduction

Biological orifices such as blood vessels and the oesophagus are essential for human life [1–3]. This

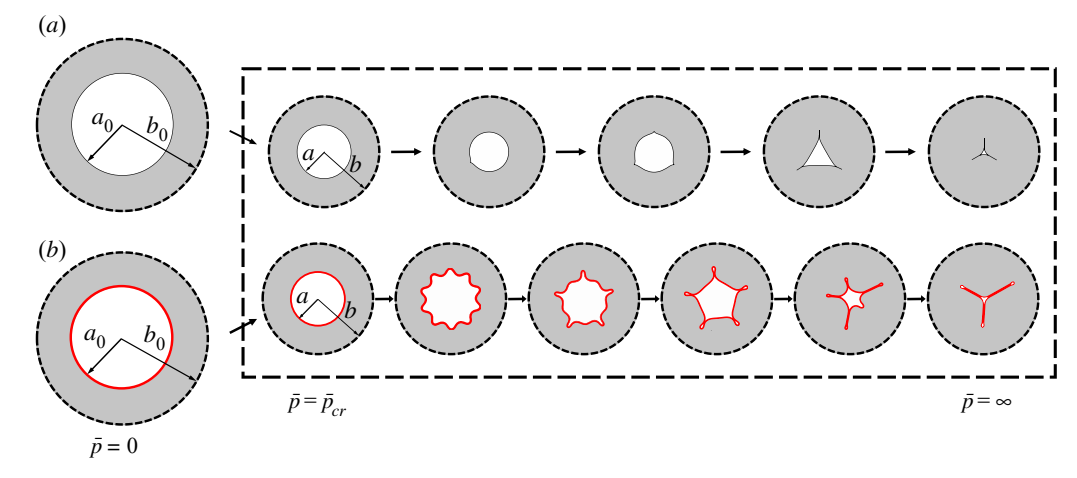


Figure 1. Schematics of the orifice closure processes with continuous ruga-phase evolutions under external pressure from $\bar{p}=0$ to $\bar{p}=\infty$; (a) the closure process of a generic orifice exhibiting creasing collapse with the threefold-symmetry mode; (b) the bilayer closure process displaying folding collapse with evolving mode; the stiffening layer is depicted by a red stripe. (Online version in colour.)

class of anatomical features serves the vital function of regulating the transition objects or material between two organs by expanding or shrinking the open cross-section of the orifice. The open area of an orifice such as a vein, which often has an initially smooth interior surface, is typically controlled by external pressure changes relative to the internal pressure. Throughout this paper, we consider the static equilibrium configuration of the orifice, and the differential external pressure will be simply denoted by external pressure. Such pressure differences in soft biological systems can occasionally induce nearly complete closure of the orifice. The closure is typically driven by time-dependent loading from muscle contraction [4], osmatic pressure [5], internal pressure drop caused by blood-flow anomalies [6] or external impact which can lead to bruising [7]. During the closure process, the orifice surface will buckle at a critical pressure, then subsequently evolve into rich post-buckling ruga [8-11] morphologies that depend on the orifice material properties and geometrical configuration [12-15]. Generic corrugated surface morphologies of the ruga structures have been experimentally observed as creases [16], singleperiod wrinkles [17], period-doubling wrinkles [18], folds [19,20], ridges and crumples [21] or crinkles [22-24]. The orifice without a stiff-surface layer (hereafter called a stiffener) evolves through a crease closure process, as shown in figure 1a; we denote the process as the generic closure process of the orifice. The orifice with a stiffener typically buckles to a surface-wrinkling mode, subsequently developing large-amplitude post-buckling ruga morphologies (figure 1b). Since various functionalities of soft-material orifices are sensitive to the evolution of these ruga morphologies, we study surface-ruga development pathways throughout the orifice closure process caused by external pressure.

Downloaded from https://royalsocietypublishing.org/ on 10 October 202

The closure process governs variation of the cross-sectional area of the orifice as a function of external pressure. The external pressure can be used to control viscous fluid flow through the orifice or configurational force exerted on a solid object in the orifice under an external pressure gradient in the axial direction. Owing to the near incompressibility of the orifice matrix, notable variations in the orifice cross-sectional area can be engendered by small displacements at the external boundary. These attractive properties of the orifice closure process, manifesting as ruga bifurcations under external pressure, provide valuable guidelines for designing functional artificial soft-material orifices. In particular, the orifice closure process governs the compressibility of soft composite materials reinforced by hollow tubes, a configuration often observed in biological systems, such as tissues surrounding blood vessels [3,25]. When an external pressure

compresses a soft-matrix composite with sparsely distributed tubes, each tube locally collapses with buckling modes of a tube in an infinite medium in a process that does not lead to global deformation instability of the matrix. By contrast, interactive collapse processes of densely distributed tubes would elicit homogenized compressibility of the composite, which can induce loss of ellipticity in its homogenized global deformation [26–29].

The orifice closure process is typically governed by ruga-phase evolution due to external pressure increases [30] or internal pressure drops generated by internal fluid-structure interactions [6]. The study of the former process has been initiated from the Timoshenko ring buckling theory [31]. Since then, the matrix-free cylindrical-shell buckling model has been extensively adopted for vein-collapse analysis. However, our analysis reveals that the closure resistance is primarily determined by the nonlinear matrix behaviour, unlike the model prediction of the matrix-free cylindrical-shell buckling. Here, we consider an individual orifice closure process in an incompressible neo-Hookean solid as a generic unit process and investigate the complete ruga-phase evolution pathways of the unit orifice closure process. The study of the unit closure process is crucial to understand the deformation instability of soft-materials that host hollow tubes. Thus, this study can inform safety assessments for human orifices and is critical to design functionally controllable soft-material orifices.

This paper provides a systematic study on the soft-material orifice closure processes under external pressure. Section 2 presents the generic orifice closure process without a stiffener, including results from both experimental and finite-element method (FEM) analyses. This section also includes a novel experiment for testing soft-material elastic modulus and an accurate projection method to identify the subcritical-limit strain at creasing from experimental and FEM analyses. Section 3 offers the analysis results on the effect of the stiffener on the orifice closure process by constructing a series of ruga-phase diagrams (RPDs) and closure-area maps. The results include an analytical expression of the critical initial-buckling pressure for an elastic stiffener with a wide range of variation in the stiffness and thickness. The results also include the construction of the pressure-dependent orifice-closure-area diagrams, which comprehensively reveal the kinematic mechanisms and the associated energetics for the post-buckling symmetrybreaking processes of the orifice closure.

2. Generic orifice closure processes of incompressible neo-Hookean solids

In this section, we investigate orifice closure processes of soft-materials under uniform external pressure. Plane-strain deformation is assumed for the analysis throughout this paper. We study generic symmetry-breaking mechanisms in the closure processes by depicting the soft-material deformations as those of incompressible neo-Hookean solids. The strain energy, W, of an incompressible neo-Hookean solid is given by Treloar [32],

$$W = \frac{\mu}{2} \sum_{i=1}^{3} (\lambda_i^2 - 1), \tag{2.1}$$

where μ is the shear modulus, and λ_i represents the principal stretches of the deformation, for which a constraint of $\lambda_1\lambda_2\lambda_3 = 1$ is imposed for incompressibility.

In the generic orifice closure process, see figure 1a, the orifice's cross-sectional area first shrinks without losing its circular-shape symmetry. At a critical pressure the circular configuration bifurcates to a lower-energy creased configuration. Here, we study how a series of such crease bifurcation processes determine the relationship between the normalized pressure, $\bar{p} = p/\mu$, and the normalized cross-sectional area, $\bar{A} = A/A_0$, for which A_0 is the initial cross-sectional area. To this end, we measure the orifice area \bar{A} as a function of the applied pressure \bar{p} , and compare the experimental results with those of finite-element simulations. We demonstrate that this orificearea measurement is a novel method of identifying the critical crease strain and the shear modulus of the soft material.

(a) Experimental analysis of the generic orifice closure processes

The experimental apparatus is shown in figure 2a. In the experiment, axisymmetric and uniform external pressure was imposed by a water-filled pressure vessel to compress an elastomer specimen with a cylindrical orifice at its centre while enforcing plane-strain conditions. The water pressure was quasi-statically controlled while imaging the orifice's cross-section with a scientific digital camera (Stingray F146B), through a clear acrylic top capping-plate. A small orifice-pressure release port was included in the bottom capping-plate. The external pressure data were recorded by a digital pressure transducer (Omega PX309-300GV). The pressure and the image data acquisitions were synchronized, and the orifice area was measured from the camera images. The cylindrical elastomer specimen with coaxial orifice was cast from a fully cured rubbery polymer (Ecoflex 00–20, Smooth-On) with small-strain shear modulus approximately 14 kPa. The cavity diameter, $2a_0$, was 6.4 mm, the outer diameter, $2b_0$, was 95.3 mm and the height was 38.1 mm. The ratio $b_0/a_0 = 15$ was sufficient to neglect the size effect from a finite specimen. Glycerine was filled in concentric ring grooves moulded on the specimen's top and bottom surfaces to lubricate the interfaces between the specimen and the top and bottom capping-plates.

We carried out five independent experiments with five different Ecoflex 00-20 samples, confirming the reproducibility of the pressure-dependent ruga-phase evolution. One set of the experimentally imaged cross-sectional shapes of the orifice under increasing pressure are shown in figure 2b. The initial circular cross-section of the orifice is shown in figure $2b_i$). When the applied pressure is sufficient to shrink the orifice diameter to $a/a_0 \approx 0.73$, for example in figure $2b_{ii}$, we observe that the cross-sectional shape remains circular but with some undulations. We believe that the undulations are caused by uneven lubrication at the interface between the specimen and the acrylic top capping-plate. At a critical pressure, the orifice surface starts to crease at three evenly spaced locations (figure $2b_{iji}$). Owing to the subcritical nature of creasing, direct identification of onset strain from experimental images may not be accurate. Therefore, we proposed a projection method to identify the critical creasing strain and pressure, which will be discussed in detail in §2c. As the pressure increases, the crease tips move into the matrix, leading to self-contact of the orifice surface adjacent to the tips (figure $2b_{iv}$). Upon further increase of the pressure up to a threshold pressure, $\bar{p} \approx 2.18$, the orifice area shrinks to $\bar{A} \approx 0.08$ in figure $2b_v$. Beyond this pressure the area remains unchanged (figure $2b_{vi}$). In the experimental case, the orifice could not completely close near the top and bottom capping-plates due to high interfacial friction above the threshold pressure, $\bar{p} \approx 2.18$. Experimentally observed cross-sectional shapes of the orifice at six different pressure levels (figure $2b_i$ – b_{vi}) are compared with those of FEM simulations in figure $2c_id$ with good agreement. Details of the FEM analysis are presented in §2b. The measured area A is plotted as a function of the pressure \bar{p} together with the results of FEM simulations in figure 2e, again with the good agreement until the closure in the experiment becomes friction-limited.

Employing the pressure, \bar{p} , measured as a function of the area A before the orifice surface creases, we can evaluate the neo-Hookean shear modulus μ of the matrix with a least-squares fit of the FEM results as

$$\mu = \frac{\int_{\bar{A}_1}^{\bar{A}_2} p_{\text{exp}} d\bar{A}}{\int_{\bar{A}_1}^{\bar{A}_2} \bar{p}_{\text{FEM}} d\bar{A}}.$$
 (2.2)

As a convenient approximation, the shear modulus can be estimated with the analytical solution of the pressure \bar{p}_{th} , for an orifice in an infinite medium of incompressible neo-Hookean solid, in place of \bar{p}_{FEM} in equation (2.2). The analytical solution of the external pressure was obtained in terms of the cross-sectional area by Zhu *et al.* [33], which leads to a non-dimensional expression,

$$\bar{p}_{th} = \frac{1}{2} \left(\frac{1}{\bar{A}} - \frac{\beta^2}{\beta^2 + \bar{A} - 1} + \ln \frac{\beta^2 + \bar{A} - 1}{\beta^2 \bar{A}} \right). \tag{2.3}$$

where $\beta = b_0/a_0$. When $\beta \to \infty$ equation (2.3) reduces to,

$$\bar{p}_{\text{th}}^{\infty} = \frac{1}{2} \left(\frac{1}{\bar{A}} - \ln \bar{A} - 1 \right) . \tag{2.4}$$

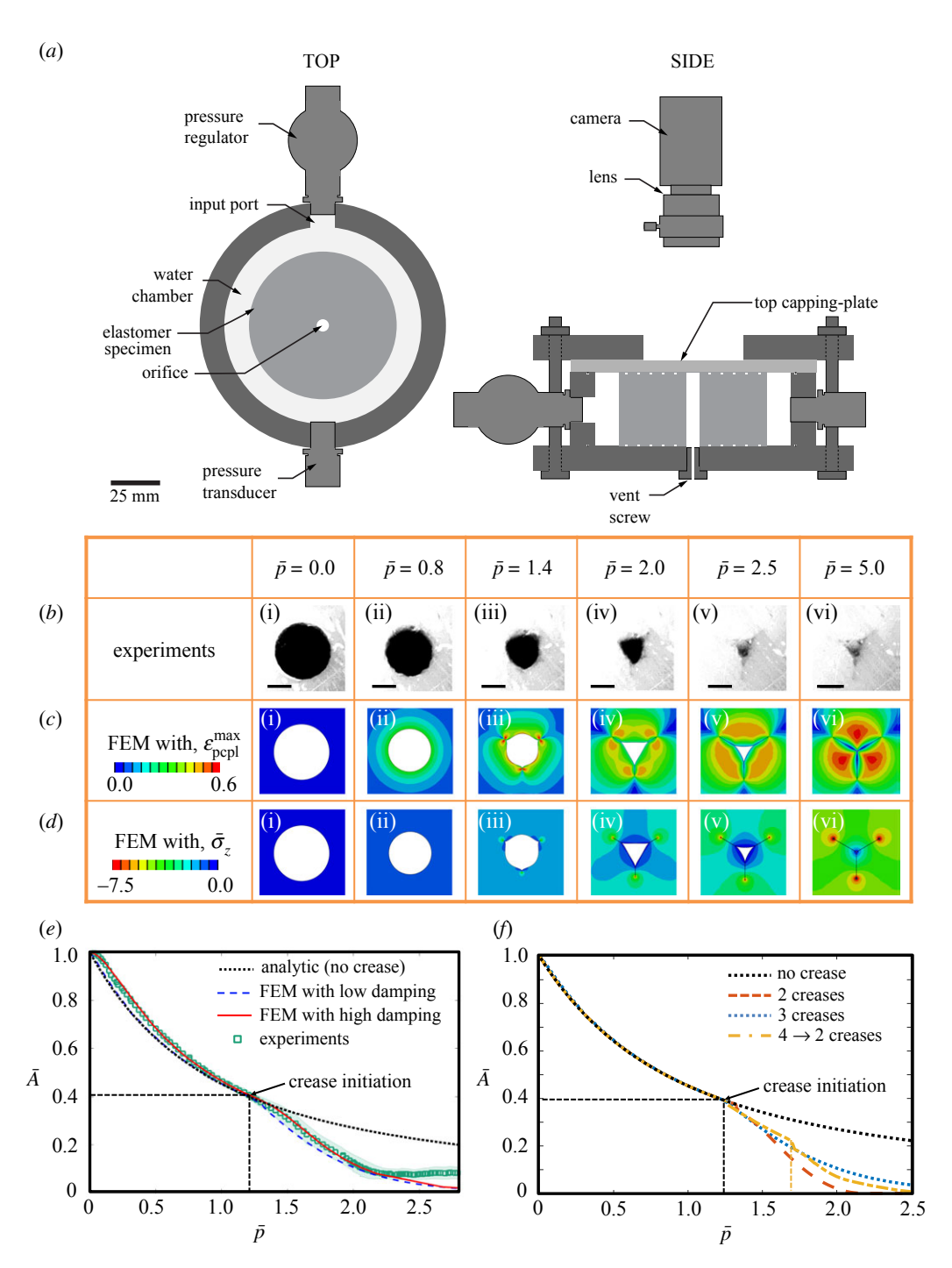


Figure 2. (a) Schematics of generic orifice closure test apparatus under plane-strain conditions; (b) experimental images of orifice cross-sections with a scale bar of 2.5 mm; FEM evaluations of (c) maximum principal logarithmic strain $\varepsilon_{\text{pcpl}}^{\text{max}}$; (d) normalized axial stress $\bar{\sigma}_z$, on the deformed configuration; (e) comparisons of normalized orifice area \bar{A} as a function of normalized pressure among analytical, FEM and experimental evaluations. The experimental data represent the mean and standard deviation of three experiments with continuous error bars (one standard deviation) shown in the shaded area; (f) comparisons of normalized area \bar{A} as a function of normalized pressure \bar{p} among three different orifice-creasing symmetries. (Online version in colour.)

The shear modulus μ of the elastomer, Ecoflex 00–20, used in our experiment is evaluated by equation (2.2) as 14.32 kPa. Simple-tension data for Ecoflex 00–20 was reported by Zhang et~al.~ [34], and the data closely fits the incompressible neo-Hookean model with $\mu=14.21$ kPa $\pm~1.00$ kPa for the tensile stretch ratio up to 2.1. The simple-tension stretch ratio 2.1 is energetically equivalent to two plane-strain stretch ratios of 0.49 and 2.03 in equation (2.1). Based on our finite-element model, the maximum in-plane principal stretch arising during the entire orifice closure process is less than 1.82, well below 2.03, as shown in figure 2c, and thus simulating the orifice closure process with an incompressible neo-Hookean model is valid and accurate. Furthermore, the minimum principal stretch at the onset of creasing is approximately 0.64, well above 0.49. Thus, the orifice-closure test based on equation (2.2) provides a convenient way of measuring the neo-Hookean shear modulus of an elastomer.

(b) FEM analysis of the generic orifice closure processes

In this subsection, we simulate the generic orifice closure processes of soft-materials with the Abaqus/Standard FEM package [35]. The soft-material is modelled as an incompressible neo-Hookean solid. The geometry of the specimen is meshed into approximately 1500 circumferential elements in five layers along the radial direction near the orifice surface, while the rest of the domain up to $R = 15a_0$ is filled with approximately 22 500 gradient-mesh elements. Those elements are plane strain 4-node bilinear hybrid elements with reduced integration (CPE4RH). All solutions reported in this paper are the final convergent solutions checked by mesh sensitivity tests. As mentioned in the previous section, our five independent experiments always exhibited crease initiation with threefold symmetry. We believe that the crease initiation caused by the three-dimensional distribution of imperfections on the orifice's interior surface allows the emergence of the lowest energy mode—the two-dimensional threefold symmetry. However, this three-dimensional crease-initiation process cannot be simulated by two-dimensional FEM analysis. Therefore, we trigger crease initiation with half-mesh-size defects as initial geometrical imperfections at three evenly spaced locations on the orifice surface in our simulation. If the imperfections were not introduced, it would crease at a local surface strain close to the Biot [36,37] critical strain of smooth-surface creasing, 0.456.

The FEM simulation results of the cross-sectional orifice morphology with associated distributions of maximum principal logarithmic strain, $\varepsilon_{\text{pcpl}}^{\text{max}}$, and axial stress, $\bar{\sigma}_z$, normalized to the shear modulus, are shown in figure $2c_id_i$, respectively. The orifice morphologies in the simulations agree well with the experimental results shown in figure 2b except for $\bar{p} > 2.18$. As we increase the pressure from the stress-free state, figure $2c_id_i$, distributions of $\varepsilon_{\text{pcpl}}^{\text{max}}$ and $\bar{\sigma}_z$ keep axi-symmetry, figure $2c_{ii}d_{ii}$, up to the onset of symmetry breaking at $\bar{p} \approx 1.20$.

At $\bar{p} \approx 1.20$, the orifice surface begins to crease at the sites of artificial imperfection, focusing $\varepsilon_{\text{pcpl}}^{\text{max}}$ and $\bar{\sigma}_z$ distributions at the crease tips. Identification of the critical creasing pressure, $\bar{p}_{\text{cr}}^{\text{FEM}} \approx 1.20$, will be discussed in detail in §2c. It is distinctly notable in figure $2c_{\text{iii}} - c_v$ and $d_{\text{iii}} - d_v$ that creasing relaxes $\bar{\sigma}_z$ along the traction-free orifice boundary of flattened or reversed curvature. At $\bar{p} \approx 2.0$, much of the open orifice surface becomes almost flat, figure $2c_{\text{iv}}$ and d_{iv} , leading to curvature reversal of the entire orifice surface. During the orifice closure process, $\varepsilon_{\text{pcpl}}^{\text{max}}$ near the orifice surface initially increases until the surface begins to crease. Subsequently, $\varepsilon_{\text{pcpl}}^{\text{max}}$ decreases beyond the creasing point. In particular, $\varepsilon_{\text{pcpl}}^{\text{max}}$ almost vanishes along curvature-reversed zones of traction-free orifice surface. As the orifice closes further, the $\varepsilon_{\text{pcpl}}^{\text{max}}$ starts to concentrate at bisecting nodes between the crease tips as seen in figure $2c_v$. The $\bar{\sigma}_z$ in each nodal region increases after the curvature reversal, figure $2d_v$. Under sufficiently large pressure, i.e. $\bar{p} = 5.0$, the orifice closes almost completely, concentrating deviatoric strain at the three bisecting nodes with the maximum principal stretch $\lambda^{\text{max}} \approx 1.81$, figure $2c_{\text{vi}}$, and focusing the axial stress $\bar{\sigma}_z$ at the crease tips, figure $2d_{\text{vi}}$. This result implies that an elastomer can fail by local tension at a bisecting node of the threefold crease, even if the orifice is hydrostatically compressed at the far-field. However, it is almost stretch free on the self-contacting orifice surface, figure $2c_{\text{vi}}$.

(c) Identification of subcritical-crease limit strain with a projection method

Owing to the subcritical nature of creasing, measuring the accurate onset strain for the creasing of an elastomer is non-trivial. Biot [36,37] evaluated the critical crease strain of a neo-Hookean solid as $\varepsilon_{\rm cr}^{\rm crease} \approx 0.456$ in his regular perturbation analysis. However, Gent & Cho [16] observed creasing at a strain, $\varepsilon_{\rm initiation}^{\rm crease} \approx 35\% \pm 7\%$, on surfaces of bent rubber strips. Afterward, Hohlfeld and colleagues [39–41] revealed that the creasing strain of Gent and Cho is close to the post-bifurcation lower-limit strain of subcritical crease, $\varepsilon_{\rm subcr}^{\rm crease} \approx 35.4\%$. Subsequently, Hong *et al.* [42] showed, in their FEM analysis, that a crease could be critically grown out of a singular imperfection, at $\varepsilon_{\rm initiation}^{\rm crease} \approx 35\%$. Recently, the initiation strain of creasing, $\varepsilon_{\rm initiation}^{\rm crease}$, on a silicone rubber surface was observed at a uniaxial-compression strain of 36% [43]. Since the crease initiation strain is sensitive to geometrical imperfections [44], and presumably to certain material properties, such as surface tension [45] and compressibility [46], it is difficult to identify the initiation strain as the post-bifurcation lower-limit strain of subcritical creasing. Therefore, here, we introduce a novel projection method of orifice compression to identify the limit strain of subcritical crease.

In this method, we assume that the local limit strain of subcritical creasing on the orifice surface hardly depends on the radius of the orifice, since the surface energy over the product of the modulus and the radius, $\gamma/\mu a_0$, is much smaller than unity. It is less than 0.02 for the orifices in our specimens. The experimental results show that the orifice compression test is an ideal method of experimentally measuring the limit strain of subcritical creasing. As shown in figure 3a of our experimental analysis, the cross-sectional area of the orifice, \bar{A} , decreases monotonically when the external pressure increases up to $\bar{p}\approx 1.2$. However, it is challenging to read out the critical creasing pressure directly from the dataset. Therefore, we only use the data with certainty in the pre-creasing range of $0.19 \leq \bar{p} \leq 1.06$ and the post-creasing range of $1.27 \leq \bar{p} \leq 2.16$ to obtain the area–pressure relations, $\bar{A}_{-}(\bar{p})$ and $\bar{A}_{+}(\bar{p})$, respectively. Then, we best fit the data to quadratic forms, $\bar{A}_{\pm}(\bar{p}) = a_{\pm}\bar{p}^2 + b_{\pm}\bar{p} + c_{\pm}$, with three coefficients each $(a_{\pm}, b_{\pm}, c_{\pm})$ in the respective regions, and extrapolate $\bar{A}_{\pm}(\bar{p})$ into the excluded range, $1.06 < \bar{p} < 1.27$, to be intersected at the crease initiation point. Then, the intersection point $(\bar{p}_{\rm cr}^{\rm exp}, \bar{A}_{\rm cr}^{\rm exp})$ is identified as the limit point of subcritical creasing, and we get $\varepsilon_{\rm cr}^{\rm exp} \approx 1 - \sqrt{\bar{A}_{\rm cr}^{\rm exp}} = 36.10\% \pm 1.44\%$ at $\bar{p}_{\rm cr}^{\rm exp} = 1.24$.

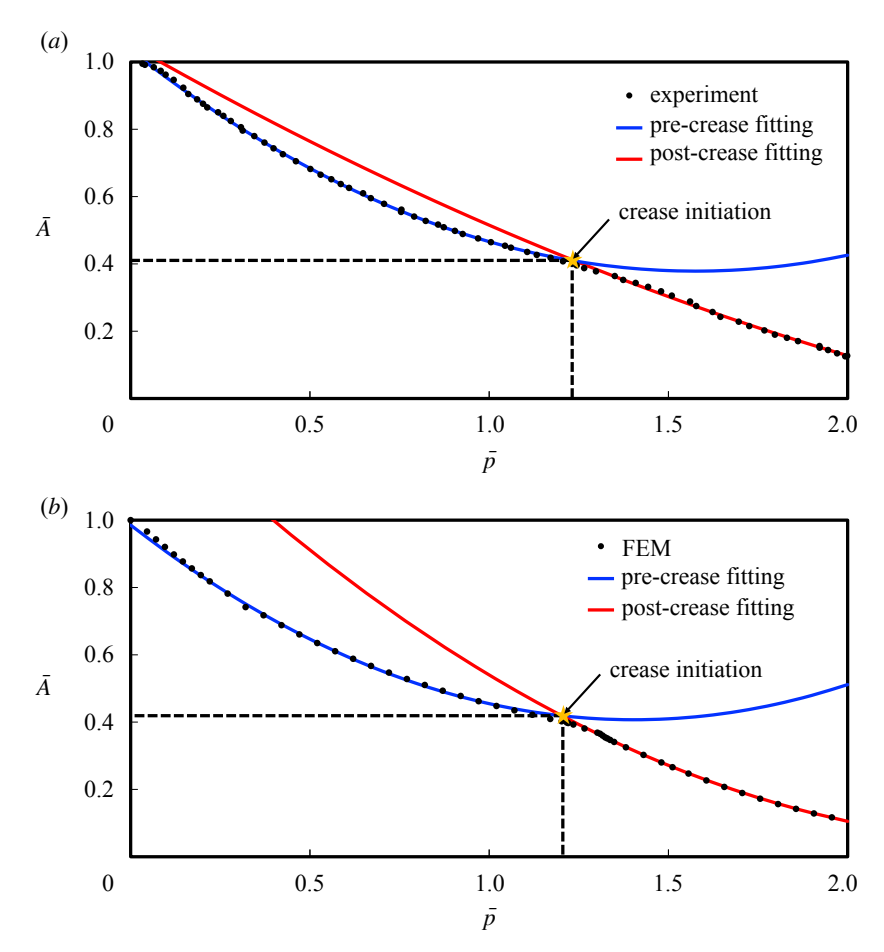


Figure 3. Novel projection method of identifying the subcritical-limit crease strain from (a) experimental and (b) FEM simulation data of the orifice-closure test, using two best-fit polynomials. (Online version in colour.)

The projection error, $\delta \varepsilon_{\rm cr}^{\rm exp}$ is evaluated from the root mean square (RMS) error of the quadratic fitting, which is provided in appendix A.

FEM evaluation using the same projection method is shown in figure 3b, which gives $\varepsilon_{\rm cr}^{\rm FEM} = 35.27\% \pm 0.54\%$ at $\bar{p}_{\rm cr}^{\rm FEM} = 1.20$. Equation (2.4) gives the critical creasing pressure of a generic orifice in an infinite medium of an incompressible neo-Hookean solid as $\bar{p}_{th} = 1.15$. The FEM analysis employed negligible viscous damping to stabilize the simulation while the experimental specimen, Ecoflex 00-20, exhibited considerable viscosity, as shown in figure 2e. Additionally, Ecoflex 00-20 is not strictly incompressible. The differences in viscosity and compressibility make the general trends of $\bar{A}_{\pm}(\bar{p})$ variations notably different between the experiment and the FEM analysis, as shown in figure 3, while respective creasing strains are very close. In other words, despite the uncertainties in incompressibility and viscosity, the experimental and FEM evaluations of the subcritical-limit strains are within the range of reported values around 35-36% [16,39,42,43].

3. The role of the stiffening layer on bilayer-orifice closure processes

In the previous section, we studied the generic orifice closure process without a stiffener and found that the orifice area during the post-creasing closure process is dependent on the multi-fold symmetry of creasing. Triggering of the multifold creasing is sensitive to imperfections in loading, orifice geometry and material properties, and thus it is difficult to control the symmetry of creasing. However, a thin layer attached to the orifice surface can regulate a multifold symmetry of wrinkling, which controls the crease modes of the matrix in the post-buckling process of the stiffened orifice. Therefore, in this section, we analyse orifice closure processes controlled by the initial wrinkling wavenumber of a thin stiffening layer with uniform thickness t and shear modulus μ_l on the orifice surface. For simplicity, in this paper, we only consider a bilayer orifice without a mismatch strain. For the sake of compact presentation of a RPD, we employ a convenient layer's compliance index, $\bar{k} = (3\mu/\mu_l)^{1/3}$ [10,47], and a normalized external pressure, $\bar{p} = p/\mu$. With this normalization, the critical pressure for various ruga-phase transitions, $\bar{p}_{\rm cr}$, becomes a function of \bar{k} and $\bar{t}(=t/a_0)$. Then, the parametric function's trajectories, $\bar{k}(\bar{p}_{cr};\bar{t})$, on the (\bar{p}_{cr}, k) plane constitute the ruga-phase boundaries on the diagram. In our FEM simulation, the embedding medium radius is chosen as $15a_0$ to approximate the infinite medium condition, where a_0 is the orifice internal radius. With this approximation, even in the final stages of the orifice closure the displacement decays rapidly along the radial direction. Nevertheless, the lowest closure mode of the displacement field persists to a small extent up to the external boundary. A small sinusoidal perturbation with amplitude 0.001 A in the radial direction is implemented on the layer surface as an initial geometric imperfection of period N to trigger the initial buckling, where the wavelength $\Lambda = 2\pi a_0/N$. We used a Fast Fourier Transform algorithm to accurately identify criticalities of all bifurcations appearing in the simulations.

(a) Ruga-phase diagrams of bilayer soft-material orifices

Extensive FEM simulations are performed to construct the RPDs for orifice systems with a stiffener under external pressure. It is known that period multiplication of large-amplitude ruga structures exhibits subtle hysteresis in morphology evolution in globally planar geometries [11]. However, our FEM analysis shows no jump of the area measure along the area—pressure-relation curve, implying that the irreversibility of the area—pressure relationship in the loading and unloading cycle is negligible. Therefore, the RPD constructed for the ruga evolution pathways with monotonic pressure increase well represents the state of orifice cross-sectional area versus pressure. From these diagrams, we can observe the effect of the stiffness mismatch and the geometry on the entire ruga-phase evolution, thus guiding our understanding of the role of the stiffener on the orifice closure process.

In a generic orifice closure process, the orifice surface without a stiffener snaps to an instantaneous-creasing mode at the critical bifurcation pressure. However, in a bilayer-orifice closure process, the thin elastic layer often wrinkles before crease initiation. The delay from wrinkling to creasing grows until the wrinkle amplitude reaches a critical value, as the stiffness ratio increases. Such delayed creasing preceded by layer wrinkling is called setback-creasing [8]. If the layer is stiff enough, the wrinkles can fold before crease initiation at the folds' troughs. Although creasing is typically preceded by wrinkling in bilayer-orifice closure processes, the wrinkle initiation pressure can be much smaller than the crease initiation pressure of the matrix's generic orifice. In turn, the matrix creasing pressure of a bilayer orifice can be lower than the crease initiation pressure of the generic orifice for specific ranges of the stiffness ratio and the thickness of the layer. In other words, particular parameter choices for the stiff layers can prematurely trigger the matrix creasing rather than stiffening the orifice. Therefore, in this subsection, we construct comprehensive RPDs of bilayer orifices to understand the entire bilayer-orifice closure processes. Our FEM simulations reveal five distinct pathways of the bilayer-orifice's morphological evolution during the orifice closure process, depending on the stiffness ratio, $\bar{\mu}_l$ (≥ 1), and the normalized thickness, \bar{t} , in the range of $1/60 \leq \bar{t} \leq 1/3$. The morphologies of the five pathways are (i) instantaneous-creasing, (ii) wrinkling/setback-creasing, (iii) wrinkling/period-doubling/creasing, (iv) wrinkling/period-doubling/folding/creasing and (v) wrinkling/period-doubling/folding. FEM simulation results for these five pathways from initial buckling to 90%-area-closure configurations for $\bar{t} = 1/40$ are shown in figure 4a. Our FEM simulations reveal that, unlike a flat bilayer ruga evolution, the surface of a neo-Hookean layer

on a curved surface of an orifice can crease after the layer folds in the orifice-ruga evolution pathway (iv).

A number of post-buckling morphologies at various pressures were computed for six different thickness ratios, $\bar{t} = 1/3$, 1/5, 1/10, 1/20, 1/40, 1/60, for $1 < \bar{\mu}_l < \infty$ (or $0 < \bar{k} = (3/\bar{\mu}_l)^{1/3} < 3^{1/3}$). Among them, the computational results of $\bar{t} = 1/5, 1/10, 1/20, 1/40$ are used to construct four different bilayer-orifice RPDs, as shown in figure 4b. The phase diagrams show that the critical pressure is sensitive to the relative layer thickness \bar{t} for a fixed compliance index k. When the thickness of the layer is relatively thin, say $\bar{t} \le 1/10$, all the five morphological pathways are distinctly observed. If the surface layer is not stiff enough, the orifice surface develops creases instead of wrinkles at a critical pressure. This critical point, which depends on \bar{t} , is denoted as w^+ in figure 4b, where \bar{k} is approximately 1.2. Within the parameter range, $1/60 \le \bar{t} \le 1/3$ and $1 \le \bar{\mu}_l$, period quadrupling did not occur, although it was observed in the primary bilayer (PB) RPD of a flat bilayer [10]. We anticipate that period quadrupling can occur in the orifice bilayer if the layer is thinner than a quadrupling thickness, $\overline{t}_q < 1/60$. The set of bilayer-orifice-ruga phases and triple points for a fixed \bar{t} is a subset of the eleven PB ruga phases with five triple points [10,11], and we were unable to find new ruga morphologies in our bilayer-orifice configurations. However, introducing mismatch strains may yield new morphologies [14,15]. A large mismatch strain can stimulate formation of ridges, instead of creases, which can transform periodic ruga morphologies into a disordered crumpling phase. The crumpling is crucial in understanding ruga morphologies of growing layers on biological surfaces.

(b) Onset of initial buckling: *surface-layer-wrinkling* versus *ring buckling*

As discussed above, the initiation of wrinkling can accelerate the orifice closure process. Therefore, understanding the initial buckling pressure will help us explore the layer's role as a stiffener during the closure process. Interestingly, the RPDs show that for every thickness ratio \bar{t} , there exists a critical compliance index k_c for which the compliance-index dependent pressure of buckling initiation exhibits its minimum value \bar{p}_{min} . When the layer becomes stiffer or softer than this critical stiffness value, it becomes more difficult to buckle the bilayer orifice. In this subsection, we derive the analytical solution of buckle-initiation pressure $\bar{p}_{bi}(\vec{k}, \bar{t})$ for bilayer orifices.

As the orifice remains circular before it buckles, application of equation (2.3) to the layer and the matrix with traction and displacement continuities at the layer/matrix interface provides the pre-buckling pressure-area relation as

$$\bar{p} = \frac{1}{2} \left[\frac{-\bar{A} + 1}{\bar{A} + (\bar{t} + 1)^2 - 1} + \ln \left\{ \frac{(\bar{t} + 1)^2}{\bar{A} + (\bar{t} + 1)^2 - 1} \right\} \right] - \frac{3}{2\bar{k}^3} \left[\frac{(\bar{t} + 1)^2}{\bar{A} + (\bar{t} + 1)^2 - 1} - \frac{1}{\bar{A}} + \ln \left\{ \frac{(\bar{t} + 1)^2 \bar{A}}{\bar{A} + (\bar{t} + 1)^2 - 1} \right\} \right].$$
(3.1)

At the onset of initial buckling of a thin surface layer, the buckle-initiation strain on the stiffening layer, $\varepsilon_{\rm bi}$, is related to the buckle-initiation compliance index, $\bar{k}_{\rm bi}$, as [10]

$$\bar{k}_{\rm bi} = 2(1 + 0.15 \,\varepsilon_{\rm bi})\sqrt{\varepsilon_{\rm bi}} \,, \tag{3.2}$$

where $\varepsilon_{\rm bi}$ is related to $\bar{A}_{\rm bi}$ as

$$\varepsilon_{\rm bi} \approx 1 - \sqrt{\bar{A}_{\rm bi}}.$$
(3.3)

Then, the buckle-initiation pressure $\bar{p}_{\rm bi}(\bar{k},\bar{t})$ for a bilayer orifice can be obtained implicitly from equations (3.1)–(3.3).

With equations (3.1)-(3.3), we can extend the experimental method introduced in §2 to evaluating the modulus of the stiffening layer with extra measurement of the layer thickness. We can first precisely measure the critical buckling area \bar{A}_{bi} and buckling pressure p_{bi}^{exp} of the orifice with the stiffener with unknown stiffness using the projection method proposed in §2c. Then we can obtain the buckle-initiation compliance index k_{bi} or the stiffness ratio $\bar{\mu}_l$ for the orifice system.

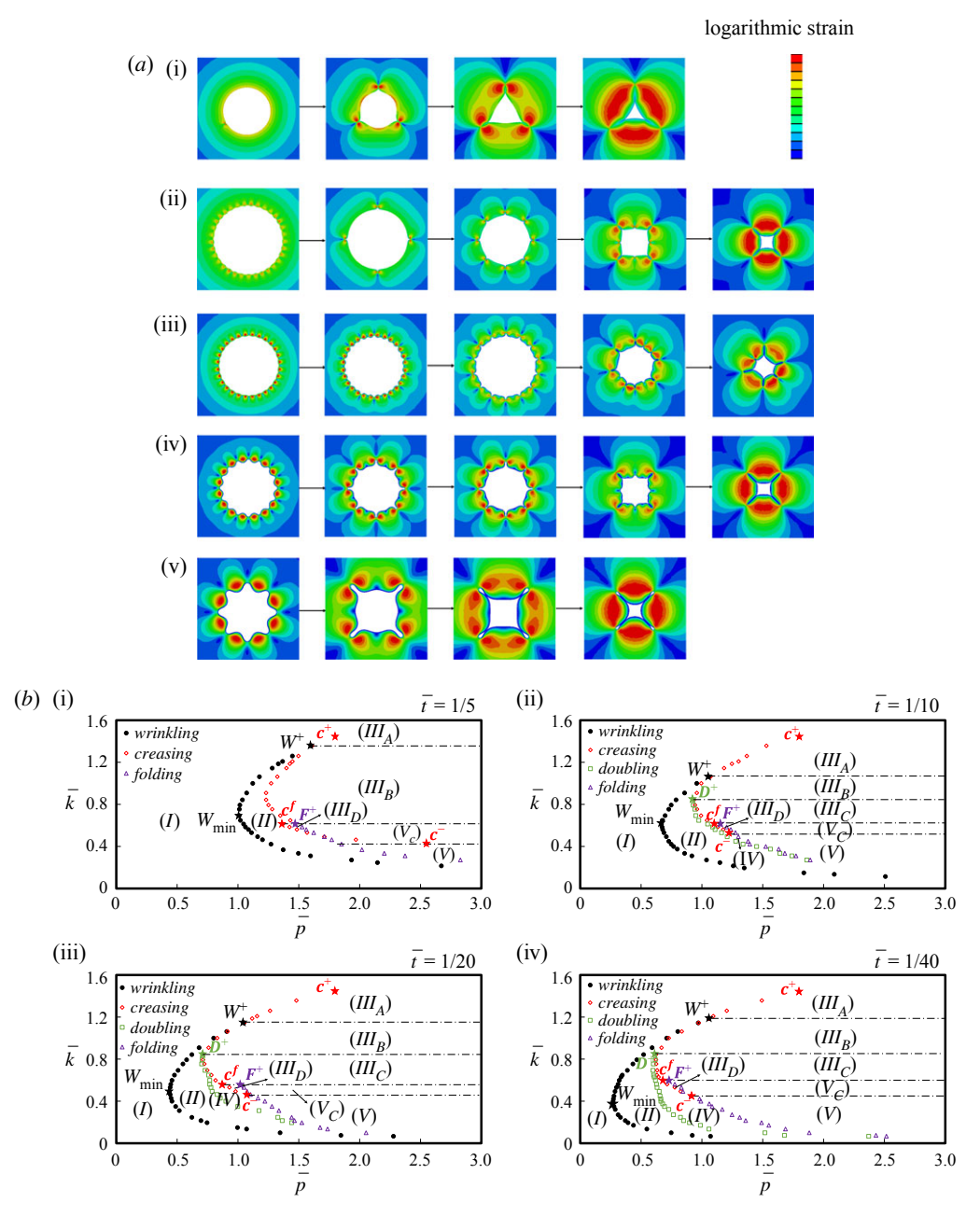


Figure 4. (a) FEM simulation results for five ruga-phase evolution pathways from initial buckling to 90%-areaclosure configurations for $\bar{t} = 1/40$. Prescribed external pressure increases from left to right, and stiffness ratio from top to bottom; (a_i) instantaneous-creasing of generic orifice $(\bar{k} = 1.44)$; (a_{ij}) wrinkling/setback-creasing $(\bar{k}=1);$ (a_{iij}) wrinkling/period-doubling/creasing $(\bar{k}=0.754);$ (a_{iv}) wrinkling/period-doubling/folding/creasing $(\bar{k}=0.45);~(a_{\rm v})$ wrinkling/period-doubling/folding $(\bar{k}=0.196).~(b)$ Ruga-phase diagrams of bilayer orifices for $\bar{t} = (b_i)$ 1/5; (b_{ii}) 1/10; (b_{iii}) 1/20; (b_{iv}) 1/40. (I) fundamental phase; (II) single-mode wrinkle phase; (III_A), (III_B), (III_C) and (III_D) four types of crease phase; (IV) double-period wrinkle phase; (V) fold phase; (V_C) fold/crease phase. The superscript '+' represents a beginning bifurcation point for a new phase; the superscript '-'represents an ending bifurcation point for a phase; W^+ , D^+ and C^{\dagger} denote three triple points. (Online version in colour.)

Finally, we can use the least-squares fit of \bar{p}_{th} , equation (3.1), and p_{exp} to find the matrix modulus μ_s , and hence obtain the modulus of the stiffener μ_f .

Now, we consider two limiting cases of buckle-initiation pressure $\bar{p}_{bi}(\bar{k},\bar{t})$. First, when the layer thickness is much smaller than the orifice radius, i.e. $\bar{t} \to 0$, the behaviour of a bilayer orifice is analogous to that of a flat PB. In this limit, the bilayer-orifice buckles in a *surface-layer* wrinkling mode, for which the buckle-initiation pressure can be derived from equation (3.1) as

$$\bar{p}_{bi}^{sl}(\bar{k}_{bi}^{sl}) = \lim_{\bar{t} \to 0} \bar{p}_{bi}(\bar{k}, \bar{t})|_{\bar{k} = \bar{k}_{bi}^{sl}} = \frac{1}{2} \left[\frac{1}{\bar{A}_{bi}} - \ln \bar{A}_{bi} - 1 \right], \tag{3.4}$$

where $\bar{A}_{\rm bi}$ is related to $\bar{k}_{\rm bi}^{\rm sl}$ through equations (3.2) and (3.3).

Second, when the layer is exceedingly stiff as $\bar{k} \to 0$, the orifice layer acts as if a rigid ring is surrounded by a soft medium subjected to hydrostatic pressure. Therefore, a *ring-buckling* mode of symmetry breaking dominates in this limit. The buckle-initiation pressure of the ring-buckling mode, $\bar{p}_{\rm bi}^{\rm rb}$ can be derived as

$$\bar{p}_{bi}^{rb}(\bar{k}_{bi}^{rb}, \bar{t}) = \lim_{\bar{k} \to 0} \bar{p}_{bi}(\bar{k}, \bar{t})|_{\bar{k} = \bar{k}_{bi}^{rb}} = \frac{3\bar{t}(\bar{t} + 2)}{2\bar{k}_{bi}^{rb}(\bar{t} + 1)^2}.$$
(3.5)

By contrast to the buckle-initiation pressure, equation (3.5), of a stiff layer on a neo-Hookean solid cavity, the mode-dependent buckling pressure of a ring under direct external pressure was traditionally analysed as

$$\bar{p}_{(n)}(\bar{k},\bar{t}) = (n^2 - 1) \left(\frac{\bar{t}}{\bar{k}}\right)^3,\tag{3.6}$$

where n is the mode number [31]. In equation (3.6), $\bar{p}_{(n)}(\bar{k},\bar{t})$ and \bar{k} are the critical buckling pressure and the compliance index normalized by an arbitrary reference modulus. The lowest ring-buckling pressure, $\bar{p}_{(2)}(\bar{k},\bar{t})$, has been often used to estimate the buckling pressure of biological orifices [3,25]. However, the buckling mode number of a biological orifice is set by matrix-property dependent \bar{k} and \bar{t} , and $\bar{p}_{(2)}(\bar{k},\bar{t})$ is much lower than $\bar{p}_{\rm bi}^{\rm rb}(\bar{k}_{\rm bi}^{\rm rb},\bar{t})$ predicted by equation (3.5), in the physically relevant range of \bar{k} and \bar{t} . If an extremely stiff layer is considered, the lowest-mode ring-buckling pressure $\bar{p}_{(2)}(\bar{k},\bar{t})$ is higher than $\bar{p}_{\rm bi}^{\rm rb}(\bar{k}_{\rm bi}^{\rm rb},\bar{t})$ of equation (3.5) in the range of $\bar{k} < \bar{t}(\bar{t} + 1)/\sqrt{\bar{t}/2 + 1}$; then, equation (3.6) is valid to get the buckling pressure.

The theoretical buckling pressure $[\bar{p}_{bi}(\bar{k},\bar{t});$ equations (3.1)–(3.3)], the surface-layer-wrinkling pressure $[\bar{p}_{bi}^{sl}(\bar{k});$ equation (3.4)], the ring buckling pressure $[\bar{p}_{bi}^{rb}(\bar{k},\bar{t});$ equation (3.5)], and the FEM predictions are plotted in figure 5a–e for five different thicknesses. The $\bar{p}_{\rm bi}(\bar{k},\bar{t})$ is consistent with the FEM results for all thicknesses considered. When the layer is relatively soft, the $\bar{p}_{\rm bi}(k,\bar{t})$ approaches the Biot limit of creasing pressure, 1.80, which can be obtained from equation (2.4) by inserting λ_{Biot}^2 in place of \bar{A} with Biot's critical creasing stretch ratio, $\lambda_{\text{Biot}} = 0.544$. The results in figure 5a–e show that $[\bar{p}_{bi}^{sl}(\bar{k});$ equation (3.4)] and $[\bar{p}_{bi}^{rb}(\bar{k},\bar{t});$ equation (3.5)] are lower bounds of $[\bar{p}_{\rm bi}(\bar{k},\bar{t})]$; equations (3.1)–(3.2)]. The results show that the layer-curvature effect on the layer's buckling resistance increases with the stiffness and thickness of the layer. When the buckling mode number decreases down to two, the buckle-initiation pressure approaches to the ringbuckling pressure $\bar{p}_{(2)}(\bar{k},\bar{t})$. For the buckling mode number greater than two, the soft matrix plays a significant role in resisting layer buckling by enforcing that the layer buckles in a higher mode. The wrinkle-mode buckling tends to decrease the buckle-initiation pressure as the compliance index, \bar{k} , decreases from $3^{1/3}$. By contrast, the ring-buckling mode increases the buckle-initiation pressure as \bar{k} decreases to approach the value ($\bar{k} \ll 1$) of mode-2 ring buckling. The two mechanisms of buckling set the minimum buckle-initiation pressure \bar{p}_{min} at a critical k_c . Understanding the conditions of getting \bar{p}_{\min} is essential to design buckle-resistant bilayer orifices. The \bar{p}_{min} and k_c are plotted in figure 5f as a function of \bar{t} . Both \bar{p}_{min} and k_c monotonically increase from zero with \bar{t} , meaning that the thinner the layer, the lower the \bar{p}_{min} and k_c will be.

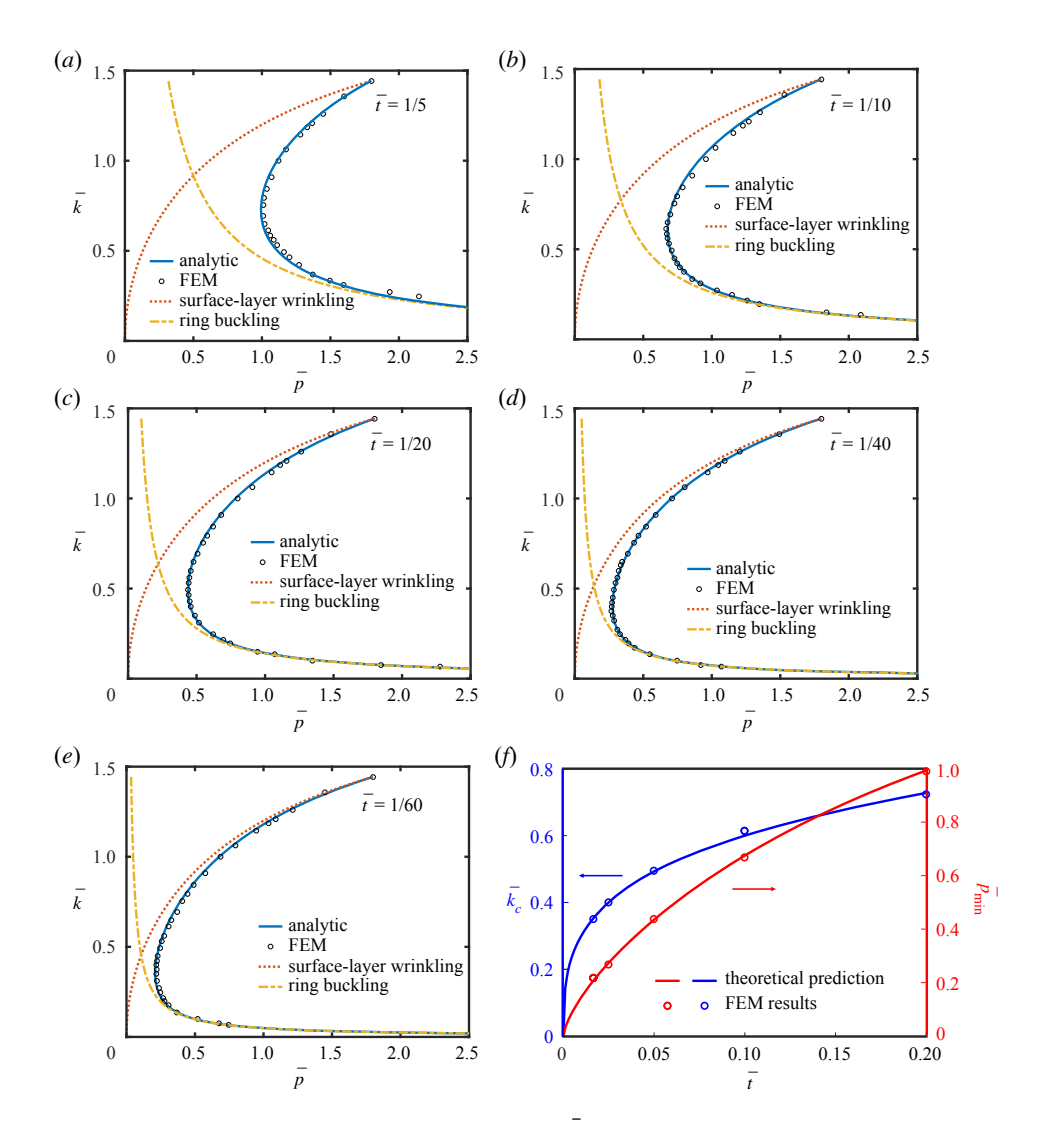


Figure 5. Buckle-initiation pressure depending on compliance index \bar{k} for different stiffener thickness \bar{t} , presented with *surface-layer-wrinkling* and *ring buckling* asymptotes: (a) $\bar{t} = 1/5$; (b) $\bar{t} = 1/10$; (c) $\bar{t} = 1/20$; (d) $\bar{t} = 1/40$; (e) $\bar{t} = 1/60$; (f) critical characteristic wavenumber \bar{k}_c and the minimum wrinkling pressure \bar{p}_{\min} as a function of stiffener thickness \bar{t} .(Online version in colour.)

(c) Post-buckling closure resistance of soft-material bilayer orifices

As shown in §3a, after the initial buckling of the stiffener, the orifice cross-sectional area is significantly reduced during subsequent symmetry-breaking orifice closure processes. To characterize the role of the stiffener on the orifice closure processes, finite-element analysis is used to construct the pressure-dependent closure-area diagrams for five different configurations, as displayed in figure 6. In each diagram, the corresponding points of \bar{p} for $\bar{A}=0.7,0.4$, and 0.1 are collected to generate 30%-, 60%- and 90%-closure contour lines. Analytical expressions of the pressure-area relations for orifice closure that keeps circular cross-sectional symmetry without symmetry breaking are plotted for $\bar{A}=0.7$, and 0.4 in dashed lines as reference lines. It is distinctly notable that buckling of the layer markedly elevates the post-buckling orifice-closure rate in the entire range of \bar{t} and \bar{k} . However, we also note that the closure rate is substantially retarded by relatively compliant layers, showing strong closure resistance.

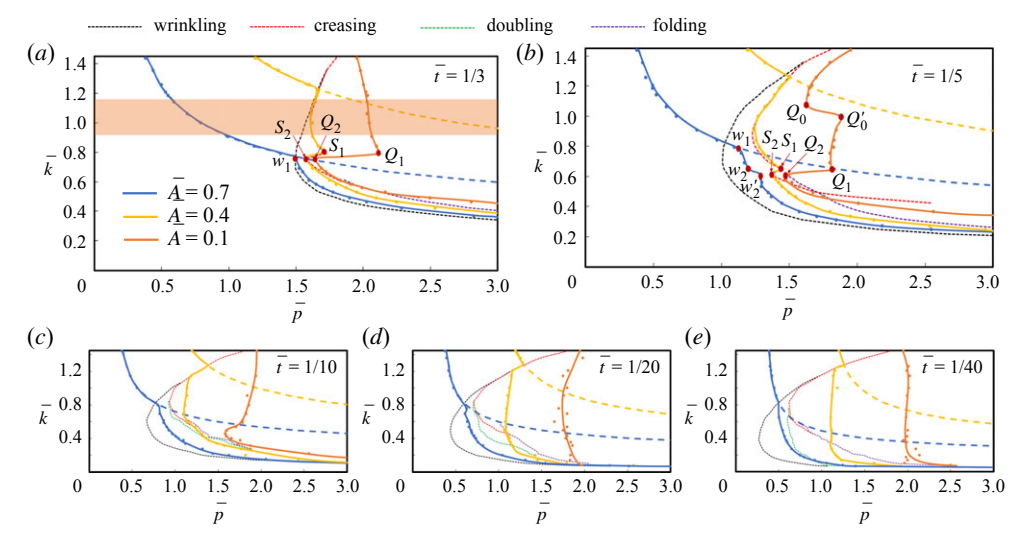
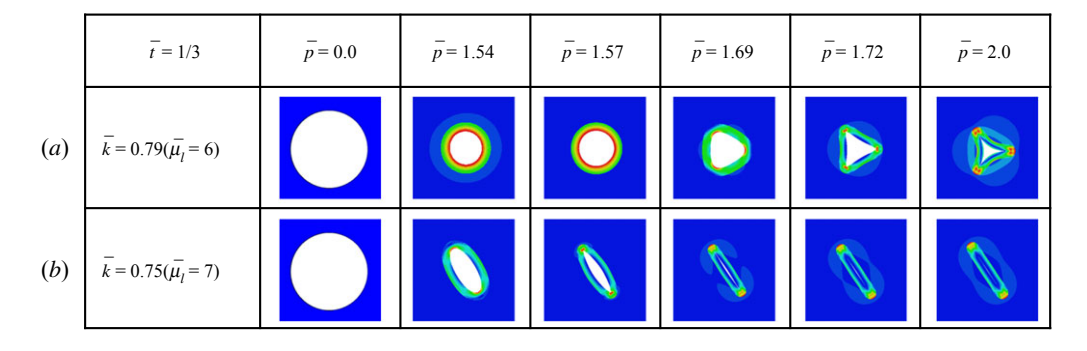


Figure 6. Pressure-dependent orifice-closure area diagrams for (a) $\bar{t}=1/3$; (b) $\bar{t}=1/5$; (c) $\bar{t}=1/10$; (d) $\bar{t}=1/20$; (e) $\bar{t}=1/40$. Discrete dots represent FEM results for $\bar{A}=0.7$, $\bar{A}=0.4$ and $\bar{A}=0.1$. Solid lines stand for contours of 30%, 60% and 90% orifice closures constructed by FEM simulations. Thick dotted lines represent theoretical pressure area relation without buckling for $\bar{A}=0.7$, and $\bar{A}=0.4$. Thin dotted lines denote ruga-phase boundaries of buckle initiation shown in figure 4. The shaded region in (a) corresponds to the \bar{k} range of the human saphenous vein system (0.924 $\leq \bar{k} \leq$ 1.186). Particular points are labelled in (a) and (b) for explanatory convenience in the main text. (Online version in colour.)

In figure 6a, contour lines of constant \bar{A} abruptly kinks at $\bar{k}\approx 0.78$ for an orifice with a thick stiffener ($\bar{t}=1/3$), kinking the contour lines of 60% and 90% closures from S_1 and Q_1 to S_2 and Q_2 , respectively. The orifice wrinkles at w_1 for $\bar{k}\approx 0.78$. In the range of $\bar{k}<0.78$, relatively stiff stiffeners significantly accelerate the area reduction rate in the post-buckling process, despite that the stiffeners delay buckling initiation to $\bar{p}_{\rm bi}>1.5$ from $\bar{p}_{\rm cr}\approx 1.2$ of the generic orifice. With \bar{k} approaching 0.78 from below, the fraction of orifice closure increases from 30% (w_1) to 90% (Q_2) with only an approximately 10% increment in external pressure. By contrast, in the range of $0.78<\bar{k}<1.44$ (or $1<\bar{\mu}_l<6$), relatively compliant stiffeners exhibit strong resistance against orifice closure. The \bar{k} range of strong closure resistance substantially varies with the stiffener thickness, as shown in figure 6b-e. In these closure resistant ranges, the orifice area \bar{A} hardly changes with \bar{k} .

The apparent closure-resistance phenomenon is caused by the final closure mode of threefold symmetry, triggered by the eigenmode of the initial layer wrinkling. Figure 7a shows the orifice configuration evolving into the final threefold symmetry for $\bar{k}=0.79$ and $\bar{t}=1/3$, exhibiting strong closure resistance in figure 6a. By contrast, the orifice collapses with twofold symmetry for $\bar{k}=0.75$ and $\bar{t}=1/3$, as shown in figure 7b, presenting negligible closure resistance in figure 6a. Similarly, for $\bar{t}=1/5$, the orifice collapses with threefold symmetry exhibiting strong closure resistance for $0.6 < \bar{k} < 1.0$, figure $7c_{\rm ii}$, but with twofold symmetry for $\bar{k} < 0.6$, figure $7c_{\rm iii}$, and $1.0 < \bar{k} < 1.44$, figure $7c_{\rm i}$, exhibiting strong resistance for the threefold symmetry. For the \bar{k} value of 0.6, the contour lines of 30%, 60% and 90% closures of the orifice kink from w_2 , v_2 , v_3 and v_4 , v_4 , v_5 , v_5 , v_5 , v_6 , $v_$

Here, as a biological example of orifice-closure resistance, we consider the functional properties of a vein, a vital orifice in the human body. A vein often experiences higher external pressure than the internal pressure, and is susceptible to buckling-induced injuries [3,25]. Taking



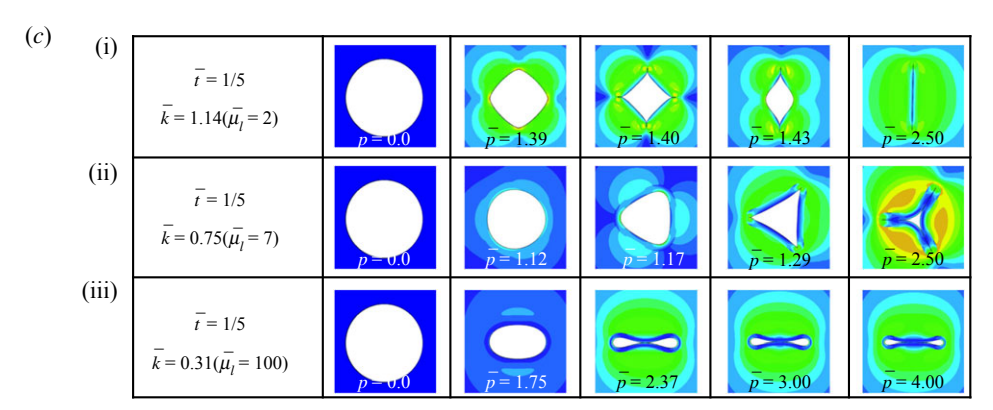


Figure 7. Orifice morphologies at various external pressure levels, collapsing with (a) threefold symmetry for $\bar{t}=1/3$ and $\bar{k}=0.79(\bar{\mu}_I=6)$, passing Q_1 in figure 6a; (b) twofold symmetry for $\bar{t}=1/3$ and $\bar{k}=0.75(\bar{\mu}_I=7)$, passing Q_2 in figure 6a. For (c), $\bar{t}=1/5$ with (c_i) $\bar{k}=1.14(\bar{\mu}_I=2)$; (c_{ij}) $\bar{k}=0.75(\bar{\mu}_I=7)$; (c_i) $\bar{k}=0.31(\bar{\mu}_I=100)$, showing collapse processes with four-fold/twofold creasing, threefold wrinkle-creasing and twofold folding symmetries correspondingly. Contours of logarithmic strain are rescaled in each plot for visualization. (Online version in colour.)

the human saphenous vein (SV) as a specific example, the measured wall thickness of the SV is $0.51\pm0.03\,\mathrm{mm}$ and the outer diameter $4.2\pm0.6\,\mathrm{mm}$ [48], which yields \bar{t} in the range of approximately 0.25 to 0.43. Thus, we select $\bar{t}=1/3$ as a representative thickness ratio of the SV. The circumferential elastic modulus of the SV at zero internal pressure is evaluated as $E_{\theta}=16.8\pm6\,\mathrm{kPa}$ from the experimental data reported in [49], for which the stress–strain relation is represented by $\sigma_{\theta}=\mu_{\theta}(\lambda_{\theta}^2-\lambda_{\theta}^{-4})$ with λ_{θ} the circumferential stretch. Then, the range of the SV's shear moduli becomes, $\mu_{\theta}=E_{\theta}/6=2.8\pm1\,\mathrm{kPa}$. The shear modulus of human tissue surrounding the SV was estimated as $\mu_{t}=1\,\mathrm{kPa}$ [50]. Thus, the typical \bar{k}_{v} range for the SV is, $0.924<\bar{k}_{v}<1.186$ ($1.8<\bar{\mu}_{l}<3.8$), which is marked in figure 6a in the shaded area. Remarkably, this \bar{k}_{v} range falls in the range of the strong closure-resistance region. The results indicate that vein-stiffening pathologies can yield 40% loss of vein's capacity to resist easy closure under external pressure.

4. Conclusion

In this paper, we have discussed the closure processes of generic and bilayer circular orifices in soft-material matrices under external pressure. As this soft-orifice deformation is steered by response-symmetry of finite elasticity, the incompressible neo-Hookean model is employed in both our theoretical and FEM analyses, which were directly compared to experimental measurements.

The theoretical and FEM analysis results on the orifice area versus pressure relation of a generic orifice closely match experimental measurements. For the experiment, an innovative orifice

closure test apparatus was designed and used to measure area and shape variations of a circular orifice in a soft elastomer as external pressure was gradually applied. During the closure process, the circular symmetry breaks when the orifice surface strain reaches approximately 0.36, and the orifice creases with threefold symmetry. The final 40% closure area strongly depends on the initial mode number of creasing. Unlike half-space surface creasing, the radially growing orifice crease is highly stable, and crease localization is limited. Consequently, metastable threefold-symmetric creasing is unwavering up to complete closure of the orifice, despite that twofold-symmetric creasing of complete closure is globally more stable. When the orifice is closed with threefold symmetry, the periphery of the orifice almost fully recovers its original length upon complete closure. In this study, we measured the neo-Hookean shear modulus and the subcritical-limit crease strain of Ecoflex 00–20 as $14.32\,\mathrm{kPa}$ and $36.10\pm1.44\%$, respectively, employing the orifice closure test and a novel projection method of data processing.

Considering a bilayer orifice, the stiffener delays or promotes symmetry-breaking bifurcation of orifice closure, depending on the compliance index \bar{k} and the thickness \bar{t} of the layer. The stiffener's initial buckling mode determines the post-buckling bilayer-orifice closure processes. To comprehensively understand the stiffener's role, we have constructed a series of bilayer RPDs in the phase plane of $(\bar{p}, \bar{k}; \bar{t})$ through FEM simulations. On the phase diagram, five typical ruga-phase evolution pathways are found. We have derived analytical solutions, equations (3.1)–(3.3), for the buckle-initiation pressure, $\bar{p}_{\rm bi}(\bar{k},\bar{t})$, which agree well with FEM solutions. The analyses reveal two limiting buckling mechanisms of surface-layer-wrinkling and ring-buckling modes, which elucidate the minimum initial buckling pressure \bar{p}_{min} . We found the matrix-free ring-buckling pressure, $\bar{p}_{(2)}(k,\bar{t})$, which has been continuously used to estimate the buckling pressure of biological orifices [3,25] is much lower than $\bar{p}_{bi}^{rb}(\bar{k}_{bi}^{rb}, \bar{t})$ which consider the physically relevant range of matrix properties. Once the stiffener buckles, post-buckling symmetry-breaking processes drastically elevate the orifice-closure rate in the entire range of k and \bar{t} . However, the closure rate is substantially retarded by relatively compliant layers, showing strong closure resistance that comes from the final closure mode of threefold symmetry. The closure resistance of final orifice collapse with threefold symmetry is substantially higher than that with the twofold symmetry employed in the conventional matrix-free cylindrical-shell buckling analyses [3,6]. Applying the ruga-mechanics theory of soft orifices developed in this paper, we found that the compliance index of human SVs, $0.924 < \bar{k}_v < 1.186$, remarkably lies in the range of the exceptionally strong closure resistance.

Data accessibility. Neo-Hookean model fitting data for Ecoflex-0020, experimental data, modulus estimation codes, post-processing codes, error analysis data and examples of FEM data are available from the Brown Digital Repository at https://doi.org/10.26300/7fc7-dp10.

Authors' contributions. H.J. carried out the FEM analysis. H.J. and A.K.L. performed the experiments. H.J. and K.-S.K. conceived and implemented the analytical models. K.-S.K. supervised the work. All authors contributed to interpret the results and draft the manuscript. All authors gave final approval for the publication.

Competing interests. We have no competing interests.

Funding. This work was supported by U.S. National Science Foundation (Awards CMMI-1563591 and 1934314, and DGE 1058262 for A.L.'s research fellowship), and Brown University for H.J.'s graduate fellowship.

Appendix A. Error analysis for identification of subcritical-crease limit strain

In this appendix, we present an error analysis in evaluating the subcritical-limit crease strain $\varepsilon_{\rm CT}$ from experimental or computational-simulation data of the soft-orifice closure test. An error function to be minimized for the errors between the quadratic fitting polynomials introduced in §2c and the dataset can be written as

$$E_{\pm} = \sum_{i=1}^{N_{\pm}} (a_{\pm}\bar{p}_i^2 + b_{\pm}\bar{p}_i + c_{\pm} - \bar{A}_i)^2, \tag{A 1}$$

where the subscripts - and + represent pre-creasing and post-creasing domains, respectively. The subscript i corresponds to the ith data point and N_{\pm} the total number of data points in the respective domains. Writing the minimizing condition, $\partial E_{\pm}/\partial a_{\pm} = \partial E_{\pm}/\partial b_{\pm} = \partial E_{\pm}/\partial c_{\pm} = 0$, into a matrix form

vields

$$M \begin{bmatrix} a_{\pm} \\ b_{\pm} \\ c_{\pm} \end{bmatrix} = Q, \tag{A 2}$$

where
$$M = \begin{bmatrix} \overline{p}_i^4 & \overline{p}_i^3 & \overline{p}_i^2 \\ \overline{p}_i^2 & \overline{p}_i^2 & \overline{p}_i \\ \overline{p}_i^2 & \overline{p}_i & 1 \end{bmatrix}$$
, and $Q = \begin{bmatrix} \overline{A}_i \overline{p}_i^2 \\ \overline{A}_i \overline{p}_i \\ \overline{A}_i \end{bmatrix}$. The overbar '—' represents the average value over all

data points in each pre- and post-crease domain, except for the variable \bar{A} which is defined as the normalized area.

Thus, the coefficient error can be expressed as

$$\begin{bmatrix} \delta a_{\pm} \\ \delta b_{\pm} \\ \delta c_{\pm} \end{bmatrix} = M^{-1} \begin{bmatrix} \overline{\delta A_i \bar{p}_i^2} \\ \overline{\delta A_i \bar{p}_i} \\ \overline{\delta A_i} \end{bmatrix}, \tag{A 3}$$

where δA_i represents the difference between the interpolation and the measured data for the ith data point of the orifice area. Then, the error in estimating the creasing orifice area can be expressed in terms of the coefficient errors in each pre- and post-creasing domain as

$$\delta \bar{A}_{\rm cr\pm} = \delta a_{\pm} \bar{p}_{\rm cr}^2 + \delta b_{\pm} \bar{p}_{\rm cr} + \delta c_{\pm}. \tag{A 4}$$

Thereafter, we can get the evaluation errors of the creasing strain by taking the variation of $\varepsilon_{\rm cr} = \sqrt{\bar{A}_{\rm cr}} - 1$ as

$$\delta \varepsilon_{\rm cr\pm} = \frac{|\delta \bar{A}_{\rm cr\pm}|}{2\sqrt{\bar{A}_{\rm cr}}}.$$
 (A 5)

Then, the total projection error in evaluating the subcritical-limit crease strain is

$$\delta \varepsilon_{\rm cr} = \sqrt{(\delta \varepsilon_{\rm cr}^{2} + \delta \varepsilon_{\rm cr}^{2})/2}.$$
 (A 6)

References

Downloaded from https://royalsocietypublishing.org/ on 10 October 2021

- 1. Meyers MA, Chen PY, Lin AY, Seki Y. 2008 Biological materials: structure and mechanical properties. *Prog. Mater. Sci.* **53**, 1–206. (doi:10.1016/j.pmatsci.2007.05.002)
- 2. Wiggs BR, Hrousis CA, Drazen JM, Kamm RD. 1997 On the mechanism of mucosal folding in normal and asthmatic airways. J. Appl. Physiol. 83, 1814–1821. (doi:10.1152/jappl. 1997.83.6.1814)
- 3. Fung YC. 1990 Biomechanics: motion, flow, stress, and growth. New York, NY: Springer.
- 4. Anrep G, Blalock A, Samaan A. 1934 The effect of muscular contraction upon the blood flow in the skeletal muscle. Proc. R. Soc. B 114, 223–245. (doi:10.1098/rspb.1934.0003)
- 5. Wheeler TD, Stroock AD. 2008 The transpiration of water at negative pressures in a synthetic tree. Nature 455, 208-212. (doi:10.1038/nature07226)
- 6. Heil M, Hazel AL. 2011 Fluid-structure interaction in internal physiological flows. Annu. Rev. Fluid Mech. 43, 141–162. (doi:10.1146/annurev-fluid-122109-160703)
- 7. Kumar V, Abbas AK, Fausta N, Aster JC. 2014 Robbins and cotran pathologic basis of disease, 9th edn. Philadelphia, PA: Elsevier.
- 8. Diab M, Zhang T, Zhao R, Gao H, Kim K-S. 2013 Ruga mechanics of creasing: from instantaneous to setback creases. Proc. R. Soc. A 469, 20120753. (doi:10.1098/rspa.2012.0753)
- 9. Diab M, Kim K-S. 2014 Ruga-formation instabilities of a graded stiffness boundary layer in a neo-Hookean solid. Proc. R. Soc. A 470, 20140218. (doi:10.1098/rspa.2014.0218)
- Zhao R, Zhang T, Diab M, Gao H, Kim K-S. 2015 The primary bilayer ruga-phase diagram I: localizations in ruga evolution. Extreme Mech. Lett. 4, 76-82. (doi:10.1016/j.eml.2015.04.006)

- 11. Zhao R, Diab M, Kim K-S. 2016 The primary bilayer ruga-phase diagram II: irreversibility in ruga evolution. *J. Appl. Mech.* 83, 091004. (doi:10.1115/1.4033722)
- 12. Lambert RK, Codd SL, Alley MR, Pack RJ. 1994 Physical determinants of bronchial mucosal folding. *J. Appl. Physiol.* 77, 1206–1216. (doi:10.1152/jappl.1994.77.3.1206)
- 13. Hrousis CA, Wiggs BJ, Drazen JM, Parks DM, Kamm RD. 2002 Mucosal folding in biologic vessels. J. Biomech. Eng. 124, 334–341. (doi:10.1115/1.1489450)
- 14. Zhao R, Zhao X. 2017 Multimodal surface instabilities in curved film-substrate structures. *J. Appl. Mech.* 84, 081001. (doi:10.1115/1.4036940)
- 15. Moulton DE, Goriely A. 2011 Circumferential buckling instability of a growing cylindrical tube. *J. Mech. Phys. Solids* **59**, 525–537. (doi:10.1016/j.jmps.2011.01.005)
- 16. Gent AN, Cho IS. 1999 Surface instabilities in compressed or bent rubber blocks. *Rubber. Chem. Technol.* **72**, 253–262. (doi:10.5254/1.3538798)
- 17. Shield TW, Kim K-S, Shield RT. 1994 The buckling of an elastic layer bonded to an elastic substrate in plane-strain. *J. Appl. Mech.* **61**, 231–235. (doi:10.1115/1.2901434)
- 18. Brau F, Vandeparre H, Sabbah A, Poulard C, Boudaoud A, Damman P. 2010 Multiple-length-scale elastic instability mimics parametric resonance of nonlinear oscillators. *Nat. Phys.* **7**, 56–60. (doi:10.1038/nphys1806)
- 19. Sun JY, Xia S, Moon M-W, Oh KH, Kim K-S. 2011 Folding wrinkles of a thin stiff layer on a soft substrate. *Proc. R. Soc. A* 468, 932–953. (doi:10.1098/rspa.2011.0567)
- 20. Brau F, Damman P, Diamant H, Witten TA. 2013 Wrinkle to fold transition: influence of the substrate response. *Soft Matter* **9**, 8177–8186. (doi:10.1039/c3sm50655j)
- 21. Zang J, Zhao X, Cao Y, Hutchinson JW. 2012 Localized ridge wrinkling of stiff films on compliant substrates. *J. Mech. Phys. Solids* **60**, 1265–1279. (doi:10.1016/j.jmps.2012.03.009)
- 22. Li R, Kothari M, Landauer AK, Cha M-H, Kwon H, Kim K-S. 2018 A new subcritical nanostructure of graphene-crinkle-ruga structure and its novel properties. *MRS Adv.* 3, 2763–2769. (doi:10.1557/adv.2018.432)
- 23. Kothari M, Cha M-H, Kim K-S. 2018 Critical curvature localization in graphene. I. Quantum-flexoelectricity effect. *Proc. R. Soc. A* 474, 20180054. (doi:10.1098/rspa.2018.0054)
- 24. Kothari M, Cha M-H, Lefevre V, Kim K-S. 2019 Critical curvature localization in graphene. II. Non-local flexoelectricity-dielectricity coupling. *Proc. R. Soc. A* 475, 20180671. (doi:10.1098/rspa.2018.0671)
- 25. Fung YC, Liu SQ. 1995 Determination of the mechanical-properties of the different layers of blood-vessels in-vivo. *Proc. Natl Acad. Sci. USA* **92**, 2169–2173. (doi:10.1073/pnas.92.6.2169)
- 26. Michel JC, Lopez-Pamies O, Castaneda PP, Triantafyllidis N. 2007 Microscopic and macroscopic instabilities in finitely strained porous elastomers. *J. Mech. Phys. Solids* 55, 900–938. (doi:10.1016/j.jmps.2006.11.006)
- 27. Lopez-Pamies O, Castaneda PP. 2006 On the overall behavior, microstructure evolution, and macroscopic stability in reinforced rubbers at large deformations: I Theory. *J. Mech. Phys. Solids* **54**, 807–830. (doi:10.1016/j.jmps.2005.10.006)
- Lopez-Pamies O, Castaneda PP. 2006 On the overall behavior, microstructure evolution, and macroscopic stability in reinforced rubbers at large deformations: II - application to cylindrical fibers. J. Mech. Phys. Solids 54, 831–863. (doi:10.1016/j.jmps.2005.10.010)
- 29. Avazmohammadi R, Castaneda PP. 2016 Macroscopic constitutive relations for elastomers reinforced with short aligned fibers: Instabilities and post-bifurcation response. *J. Mech. Phys. Solids* **97**, 37–67. (doi:10.1016/j.jmps.2015.07.007)
- 30. Fung YC. 2013 Biomechanics: circulation. New York, NY: Springer Science & Business Media.
- 31. Timoshenko SP. 1961 Theory of elastic stability. New York, NY: McGraw-Hill.
- 32. Treloar LRG. 1948 Stresses and birefringence in rubber subjected to general homogeneous strain. *Proc. Phys. Soc.* **60**, 135–144. (doi:10.1088/0959-5309/60/2/303)
- 33. Zhu Y, Luo XY, Ogden RW. 2010 Nonlinear axisymmetric deformations of an elastic tube under external pressure. *Eur. J. Mech. A-Solid* **29**, 216–229. (doi:10.1016/j.euromechsol. 2009.10.004)
- 34. Zhang Q, Roach DJ, Geng L, Chen H, Qi HJ, Fang D. 2018 Highly stretchable and conductive fibers enabled by liquid metal dip-coating. *Smart Mater. Struct.* **27**, 035019. (doi:10.1088/1361-665X/aaaba3)
- 35. ABAQUS user's manual, version 6.14. 2014.
- 36. Biot MA. 1963 Surface instability of rubber in compression. *Appl. Sci. Res.* **12**, 168–182. (doi:10.1007/bf03184638)

- 37. Biot MA. 1965 Mechanics of incremental deformation. New York, NY: Wiley.
- 38. Cai S, Bertoldi K, Wang H, Suo Z. 2010 Osmotic collapse of a void in an elastomer: breathing, buckling and creasing. *Soft Matter* **6**, 5770–5777. (doi:10.1039/c0sm00451k)
- 39. Hohlfeld EB. 2008 Creasing, point-bifurcations, and the spontaneous breakdown of scale-invariance. PhD thesis, Harvard University, Cambridge, MA.
- 40. Hohlfeld E, Mahadevan L. 2011 Unfolding the sulcus. *Phys. Rev. Lett.* **106**, 105702. (doi:10.1103/PhysRevLett.106.105702)
- 41. Hohlfeld E, Mahadevan L. 2012 Scale and nature of sulcification patterns. *Phys. Rev. Lett.* **109**, 025701. (doi:10.1103/PhysRevLett.109.025701)
- 42. Hong W, Zhao X, Suo Z. 2009 Formation of creases on the surfaces of elastomers and gels. *Appl. Phys. Lett.* **95**, 111901. (doi:10.1063/1.3211917)
- 43. Tang S, Gao B, Zhou Z, Gu Q, Guo T. 2017 Dimension-controlled formation of crease patterns on soft solids. *Soft Matter* **13**, 619–626. (doi:10.1039/c6sm02013e)
- 44. Cao Y, Hutchinson JW. 2012 From wrinkles to creases in elastomers: the instability and imperfection-sensitivity of wrinkling. *Proc. R. Soc. A* 468, 94–115. (doi:10.1098/rspa.2011.0384)
- 45. Chen D, Cai S, Suo Z, Hayward RC. 2012 Surface energy as a barrier to creasing of elastomer films: an elastic analogy to classical nucleation. *Phys. Rev. Lett.* **109**, 038001. (doi:10.1103/PhysRevLett.109.038001)
- 46. Wong WH, Guo TF, Zhang YW, Cheng L. 2010 Surface instability maps for soft materials. *Soft Matter* **6**, 5743–5750. (doi:10.1039/c0sm00351d)
- 47. Cao Y, Hutchinson JW. 2012 Wrinkling phenomena in neo-Hookean film/substrate bilayers. *J. Appl. Mech.* **79**, 031019. (doi:10.1115/1.4005960)
- 48. Hamedani BA, Navidbakhsh M, Tafti HA. 2012 Comparison between mechanical properties of human saphenous vein and umbilical vein. *Biomed. Eng. Online* 11, 59. (doi:10.1186/1475-925X-11-59)
- 49. Wesly RL, Vaishnav RN, Fuchs JC, Patel DJ, Greenfield JC. 1975 Static linear and nonlinear elastic properties of normal and arterialized venous tissue in dog and man. *Circ. Res.* 37, 509–520. (doi:10.1161/01.RES.37.4.509)
- 50. Karpiouk AB, Aglyamov SR, Ilinskii YA, Zabolotskaya EA, Emelianov SY. 2009 Assessment of shear modulus of tissue using ultrasound radiation force acting on a spherical acoustic inhomogeneity. *IEEE T. Ultrason. Ferr.* **56**, 2380–2387. (doi:10.1109/TUFFC.2009.1326)